ACS APPLIED MATERIALS & INTERFACES
Research Article
www.acsami.org

Robust Two-Photon Visualized Nanocarrier with Dual Targeting Ability for Controlled Chemo-Photodynamic Synergistic Treatment of Cancer

Hao Wan,[†,‡] Yi Zhang,[†] Weibing Zhang,*[,‡] and Hanfa Zou*[,†]

[†]Key Lab of Separation Sciences for Analytical Chemistry, National Chromatographic R&A Center, Dalian Institute of Chemical Physics, Chinese Academy of Sciences, 457 Zhongshan Road, Dalian 116023, China

[‡]Shanghai Key Laboratory of Functional Materials Chemistry, East China University of Science and Technology, Shanghai 200237, China

Ⓢ *Supporting Information*

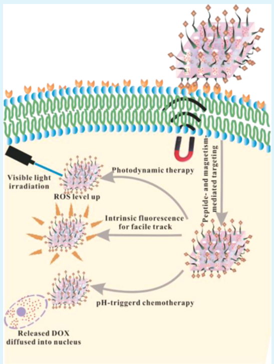

ABSTRACT: In consideration of the intrinsic complexity of cancer, just being a delivery nanovehicle for the nanocarrier is no longer enough to fulfill requirements of dealing with cancer. In this regard, the multifunctional nanocarrier appears to be an appealing choice in cancer treatment. Herein, the novel multifunctional nanocarrier (Fe_3O_4-NS-C_3N_4@mSiO_2-PEG-RGD) possessing properties of dual targeting (the peptide- and magnetism-mediated targeting), imaging (one- and two-photon modes), pH-triggered release of loaded anticancer drug, and synergistic treatment (photodynamic therapy (PDT) combined with chemotherapy) are successfully developed. The nanocarrier specifically centralizes within cancer cells with the enhanced amount through the dual targeting ability and is facilely tracked under one- and two-photon imaging modes attributed to the autofluorescence. Then, visible light irradiation-induced PDT combined with low pH-triggered chemotherapy synergistically cooperate to efficiently kill cancer cells. Following the above process, the multifunctional nanocarrier demonstrates effective inhibition of the growth of A549 and HeLa cancer cells. The efficient manipulation of Fe_3O_4-NS-C_3N_4@mSiO_2-PEG-RGD also implies potential applications of the multifunctional nanocarrier in delivery of different agents. Furthermore, it might also broaden the scope of fabrication of the multifunctional nanocarrier for inhibiting the growth of cancer cells.

KEYWORDS: *two-photon imaging, dual targeting, pH-triggered release, chemo-photodynamic synergistic treatment, multifunctional nanocarrier*

1. INTRODUCTION

The intricate properties of cancer require a high demand for the nanocarrier, which makes the integration of various functions into one single nanoplatform imperative.[1−3] In this regard, the multifunctional nanocarrier possessing targeting, imaging, stimuli response, and synergistic treatment appears to be an appealing alternative to combat cancer, not only for the enhanced uptake by cancer cells accompanied by minimization of the damage to normal cells and facile track of the nanocarrier distribution with simultaneous lighting of the lesion part to optimize the therapeutic scenario, but also for the enhanced therapeutic efficacy compared with the sole therapeutic modality. Dual targeting combining the peptide- and magnetism-mediated targeting exhibits a better way to specifically centralize the nanocarrier within cancer cells with the enhanced amount. Under the magnetic attraction, the nanocarrier would directionally and specifically approach the lesion part, followed by the peptide and magnetism promoting internalization of the nanocarrier, which in turn will enhance the therapeutic efficacy and also attenuate potential side effects toward normal cells to the greatest extent.[4−6] Because of its high resolution, precision, sensitivity, and ability to visualize real-time dynamics, fluorescent imaging is a preferred choice in cancer treatment.[7,8] However, conventional fluorescent probes with photobleaching, toxicity, and tedious steps of anchoring to the nanocarrier are mostly imaged under one-photon excitation, exhibiting limited tissue penetration, strong interference from intracellular fluorescence of the biological matrix, and potential phototoxicity, seriously affecting the practical application.[9−11] In contrast, two-photon imaging activated by the longer wavelength of light demonstrates higher spatial resolution, less photobleaching and photodamage, as well as deeper tissue penetration, more suitable for the biological imaging and sensing.[12−16] Therefore, the fluorescent nanomaterial excited by two-photon light appears to be an excellent substrate for the construction of the multifunctional nanocarrier. Meanwhile, as the ideal nanocarrier, the release of loaded drug should be specifically manipulated to make the administration of cancer on-demand, enhancing the therapeutic efficacy as well as attenuating potential side effects to normal cells.[17−19] Among all stimuli, pH is meant to be an excellent internal stimulus to trigger the release of drug attributed to the universal lower pH

Received: February 6, 2015
Accepted: April 20, 2015
Published: April 20, 2015

DOI: 10.1021/acsami.5b01165
ACS Appl. Mater. Interfaces 2015, 7, 9608−9618

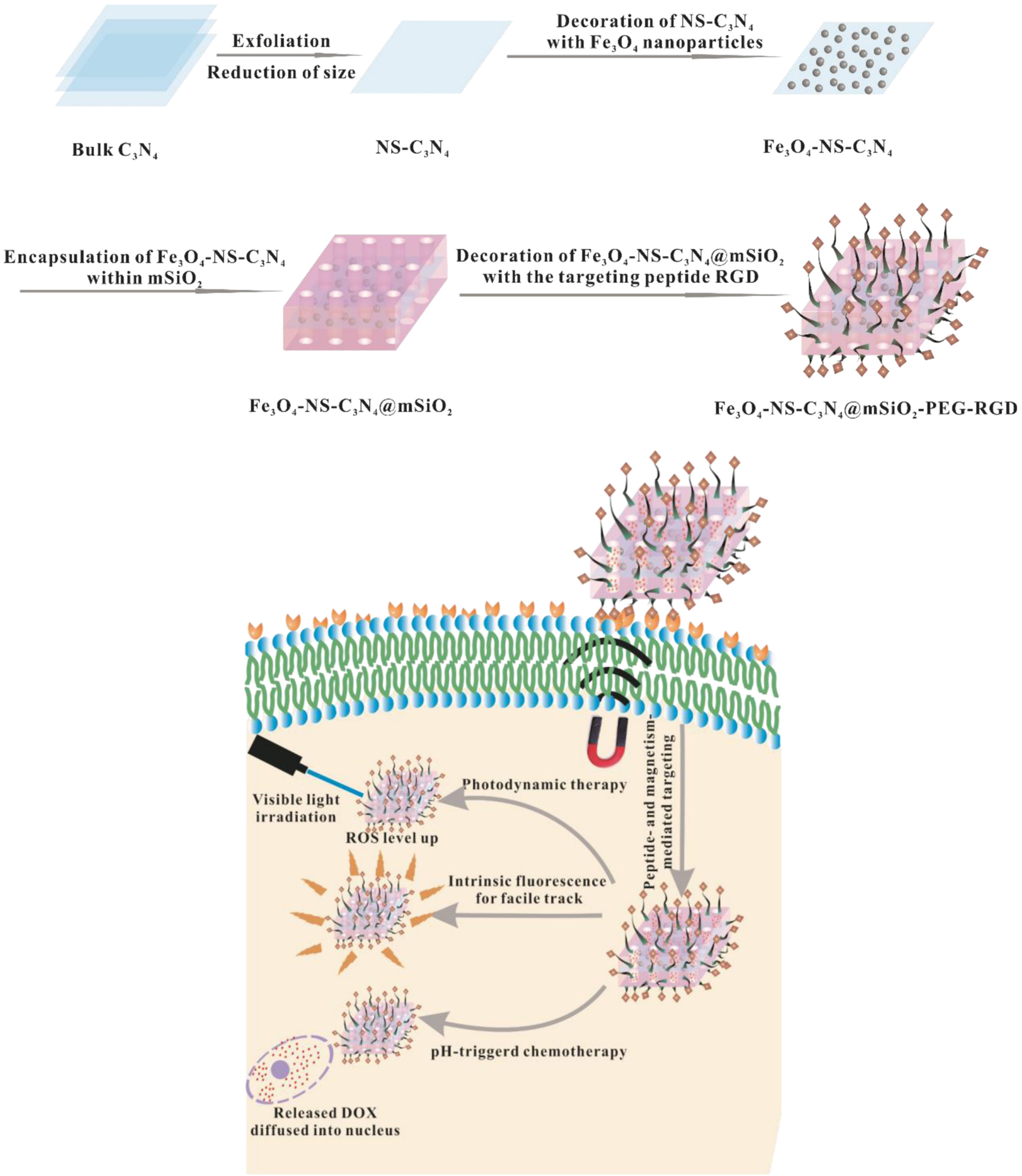

Figure 1. Schematic illustration of the fabrication process of Fe_3O_4-NS-C_3N_4@$mSiO_2$-PEG-RGD and its intracellular application.

(4.5−5.5) within cancer cells compared with normal cells, available for most kinds of cancer issues.[20−22] Normally, chemotherapy, applying toxic drug against cancer cells, is the conventional way to deal with cancer. In order to attenuate side effects, the amount of applied drug should be strictly controlled to a low extent, and the drug resistant ability of some cancer cells could weaken the potency of the drug, both of which lead to inferior chemotherapy.[23,24] Photodynamic therapy (PDT), utilizing ROS generated under light irradiation to efficiently kill cancer cells, has sparked increasing attention recently. The noninvasive therapeutic modality enables spatiotemporal treatment with high efficacy but less morbidity and disfigurement.[25−27] Therefore, synergistic treatment combining both chemotherapy and PDT appears to be a promising way to exploit each other's merits for the enhancement of the overall therapeutic effect.[28−30] Given all of the above, the fabrication of the two-photon visualized nanocarrier with the dual targeting ability for controlled chemo-photodynamic synergistic treatment would be attractive in cancer therapy.

As an analogue of graphite, graphitic-phase carbon nitride (g-C_3N_4) possesses a stacked 2D structure. Recently, g-C_3N_4 has been successfully exfoliated by polar water under ultrasonication, and the obtained C_3N_4 nanosheets (NS-C_3N_4) with enhanced fluorescent emission and photocatalytic performance have been applied in the fluorescent detector, in visible light-induced degradation, and in biological imaging.[10,31−33] The negligible cytotoxicity plus low photobleaching have enabled NS-C_3N_4 to be an excellent imaging agent. Moreover, the high cross-section of two photons also made NS-C_3N_4 visualized under the longer wavelength of light, which is more suitable in cancer treatment because of deeper tissue penetration and less interference from intracellular fluorescence of the biological matrix.[34] Meanwhile, the efficient generation of ROS under visible light irradiation also renders NS-C_3N_4 as a potential PDT agent.[35] It was reported that the decoration of NS-C_3N_4 with metal or metal oxide nanoparticles would to some extent enhance the efficacy of generation of ROS under visible light irradiation through the increase of separation efficiency of photogenerated electron−hole pairs,[36] which herein we assume would benefit the PDT effect.[32,37,38] Among these decorations, Fe_3O_4 nanoparticles seem to be a better choice attributed to an additional arrival of the magnetic response to endow the nanocomposite with a magnetic targeting ability. However, the strongly negative surface is detrimental to the uptake of Fe_3O_4-NS-C_3N_4 by cancer cells whose membrane surface is also negative, and the poor modification also limits the manipulation, both of which still hinder the further intracellular application of Fe_3O_4-NS-C_3N_4.

Due to easy modification, negligible cytotoxicity, high surface area, and excellent stability, mesoporous silica has been widely employed in the biological field.[39,40] Therefore, the coating of Fe_3O_4-NS-C_3N_4 with a mesoporous silica shell (Fe_3O_4-NS-C_3N_4@mSiO_2) is meant to enhance the feasibility of being an elaborate drug delivery system. As the novel nanocarrier, Fe_3O_4-NS-C_3N_4@mSiO_2 displays certain distinct merits: (1) vertical pore channels of the mesoporous silica shell and the interaction between anticancer drug and NS-C_3N_4 would together contribute to a high loading capacity; (2) the coating of Fe_3O_4-NS-C_3N_4 with the mesoporous silica shell not only enhances the dispersibility and stability of the nanocarrier in the physiological condition but also amplifies the ability for further modification; (3) the autofluorescence of NS-C_3N_4 would enable the facile track of the nanocarrier distribution with simultaneous imaging of the lesion part; (4) the capacity of generation of ROS under visible light irradiation could realize PDT which would combine with chemotherapy to synergistically treat cancer with the enhanced therapeutic efficacy; (5) the modest magnetic response would endow the nanocarrier with a magnetic targeting ability.

A targeting molecule (aptamer, antibody, peptide, etc.), showing specifically a high affinity toward certain receptors overexpressed on the membrane surface of cancer cells, has been anchored onto various nanocarriers for the enhanced uptake by cancer cells and minimization of potential side effects to normal cells. Among these molecules, an integrin-binding cell adhesive peptide, arginine-glycine-aspartic acid motif (RGD), has sparked a variety of interests for its universality. RGD is a three-amino-acid sequence with high affinity toward integrin $\alpha_v\beta_3$, a tumor angiogenesis biomarker that is up-regulated on tumor endothelial cells and many types of tumor cells.[41−43] Because of this special property, RGD coupled with Fe_3O_4-NS-C_3N_4@mSiO_2 would better fulfill requirements of the multifunctional nanocarrier for cancer treatment.

Herein, for the first time the two-photon visualized nanocarrier with the dual targeting ability for controlled chemo-photodynamic synergistic treatment of cancer was successfully developed. The multifunctional nanocarrier enabled the facile track of the delivery process under one- and two-photon imaging attributed to the autofluorescence and selectively targeted cancer cells contributed from the combination of the peptide- and magnetism-mediated targeting. The dual targeting ability also enhanced the uptake of the nanocarrier by cancer cells, which in turn improved the therapeutic efficacy. The efficient cancer treatment was realized by low pH-triggered chemotherapy coupled with visible light irradiation-induced PDT. With all these advances integrated into one single nanoplatform, the multifunctional nanocarrier is presented to be an excellent drug delivery system in dealing with cancer (Figure 1).

2. EXPERIMENTAL SECTION

2.1. Materials. Hexadecyltrimethylammonium bromide (CTAB), melamine, tetraethyl orthosilicate (TEOS, 99%), and (3-aminopropyl)triethoxysilane (APTEOS, 99%) were purchased from Sigma-Aldrich (St. Louis, MO). RPMI 1640 medium and bovine serum were obtained from Invitrogen (Carlsbad, CA). Ammonium nitrate, ferric chloride, ethylene glycol, sodium hydroxide, isopropanol, and ethanol were obtained from Tianjin Kermel Chemical Reagent (Tianjin). Doxorubicin in the form of hydrochloride salt was purchased from Aladdin Corporation (Shanghai). Maleimide-PEG3500-NHS was purchased from Avanti Polar Lipids Incorporation (Alabaster, AL). c(RGDfC) was purchased from GL Biochem Ltd. (Shanghai). Deionized water used for all experiments was purified with a Milli-Q water system.

2.2. Preparation of Fe_3O_4-NS-C_3N_4@mSiO_2-PEG-RGD. Bulk C_3N_4 was obtained by heating 20 g of melamine at 600 °C for 2 h in air with the ramp rate of 3 °C/min for both heating and cooling processes. To obtain C_3N_4 nanosheets (NS-C_3N_4), 1 g of bulk C_3N_4 was dispersed in 100 mL of water and sonicated for 6 h at 160 W. The resultant solution was then centrifuged at 5000 rpm for 1 h to remove large and residual unexfoliated C_3N_4 sheets. The determined amount of $FeCl_3 \cdot 6H_2O$ (10, 20, and 30 mg), 20 mg of NS-C_3N_4, and 30 mL of DEG were homogeneously dispersed under sonication for 1 h. Then, 20 mg of CH_3COONa was mixed with the above solution. The whole system was transferred into a Teflon autoclave encapsulated within a stained steel container and heated at 190 °C for 4 h. After a washing step with water and ethanol with the help of a magnet, the resulting product was designated as Fe_3O_4-NS-C_3N_4. The obtained Fe_3O_4-NS-C_3N_4 was dispersed homogeneously in a mixture of 3.74 g of CTAB and 180 mL of water. The pH of the whole system was adjusted to 11.8 by NaOH or HCl. After mechanical stirring at 80 °C for 30 min, a mixture of 0.5 mL of TEOS and 2 mL of ethanol was added dropwise. The whole system reacted for another 24 h to assemble a mesoporous silica shell onto Fe_3O_4-NS-C_3N_4. After a washing step with water and ethanol with the help of a magnet, the obtained product was designated as Fe_3O_4-NS-C_3N_4@mSiO_2. To immobilize the targeting peptide onto Fe_3O_4-NS-C_3N_4@mSiO_2, APTEOS (1 mL) was added dropwise into the isopropanol solution of Fe_3O_4-NS-C_3N_4@mSiO_2. After the solution was mechanically stirred for 24 h at room temperature, amine-modified Fe_3O_4-NS-C_3N_4@mSiO_2 was isolated, followed by two washes with isopropanol. The surfactant (CTAB) occupied in the mesoporous channels was extracted with ammonium nitrate ethanolic solution twice at 65 °C. A 10 mg portion of Fe_3O_4-NS-C_3N_4@mSiO_2-NH_2 was then treated with the PBS buffer containing 25 mg of NHS-PEG-MAL (M_w = 3500). After reaction at room temperature for 2 h, the product (Fe_3O_4-NS-C_3N_4@mSiO_2-PEG-MAL) was collected by centrifugation and washed with water twice. Finally, 2.5 mg of c(RGDfC) was reacted with Fe_3O_4-NS-C_3N_4@mSiO_2-PEG-MAL in the PBS buffer for another 4 h at room temperature (Fe_3O_4-NS-C_3N_4@mSiO_2-PEG-RGD). The final product was washed with water several times and dried at room temperature for further use.

2.3. pH-Triggered Release of DOX from Fe_3O_4-NS-C_3N_4@mSiO_2-PEG-RGD. For the loading process, each centrifugation tube containing a determined amount of DOX, 0.1 mg of Fe_3O_4-NS-

C_3N_4@mSiO_2-PEG-RGD, and 1 mL of PBS buffer (pH = 7.4) was vibrated for 24 h at room temperature in the dark. After that, the nanocarrrier was washed twice by the PBS buffer to remove DOX adsorbed on the outlet of Fe_3O_4-NS-C_3N_4@mSiO_2-PEG-RGD. Finally, these tubes were centrifuged at 20 000 *g* for 5 min to collect precipitates.

For the pH-triggered release, the release process was initiated by adding 1.5 mL of PBS buffer (pH = 4.5, 5.5, or 7.4) into each tube with a gentle vibration. At a given time, one tube was taken out and centrifuged at 20 000 *g* to collect the supernatant for the determination of the released amount of DOX by UV−vis analysis.

2.4. Confocal Laser Scanning Microscopy (CLSM) Imaging-Based Evaluation of the Dual Targeting Ability of Fe_3O_4-NS-C_3N_4@mSiO_2-PEG-RGD. A549 cancer cells were seeded at the number of 1×10^5 per well and incubated for 24 h. Two sets of cells were incubated with Fe_3O_4-NS-C_3N_4@mSiO_2-PEG and Fe_3O_4-NS-C_3N_4@mSiO_2-PEG-RGD, respectively, for 3 or 6 h. In parallel, a third set of cells was incubated with Fe_3O_4-NS-C_3N_4@mSiO_2-PEG-RGD under the magnetic attraction. After the nanocarrier not uptaken by cells was washed out with the PBS buffer, the nanocarrier within cells was excited under 405 nm for one-photon imaging and 780 nm for two-photon imaging.

2.5. Flow Cytometry Assay. A549, MCF-7, and HK-2 cells were seeded at the number of 1×10^6 per well and incubated for 24 h. For each case, two sets of cells were incubated with Fe_3O_4-NS-C_3N_4@mSiO_2-PEG and Fe_3O_4-NS-C_3N_4@mSiO_2-PEG-RGD, respectively, at a determined time. In parallel, a third set of cells was incubated with Fe_3O_4-NS-C_3N_4@mSiO_2-PEG-RGD under the magnetic attraction. After wash out of the nanocarrier not uptaken by cells with the PBS buffer, cells were collected from the well with the help of tryptic digestion. Finally, the intracellular fluorescence was detected by flow cytometry.

2.6. Detection of Intracellular ROS Level. A549 cancer cells were seeded at the number of 3×10^5 per well and incubated for 15 h. Then, Fe_3O_4-NS-C_3N_4@mSiO_2-PEG-RGD at the concentration of 60 ug/mL was added, followed by another 6 h of incubation. After Fe_3O_4-NS-C_3N_4@mSiO_2-PEG-RGD not uptaken by cells was removed by three PBS buffer washes, cells were subsequently immersed in 10 μM DCFH-DA solution for 30 min. After being with the PBS buffer to remove the residual DCFH-DA, cells divided into two groups were irradiated with visible light (450 nm) at the laser power of 40 mW/cm^{-2} or not for 10 min. The ROS level was then investigated by confocal laser scanning microscopy (CLSM) imaging.

For site-targeted PDT, after sufficient incubation with Fe_3O_4-NS-C_3N_4@mSiO_2-PEG-RGD and subsequent DCFH-DA, A549 cancer cells were irradiated at the specific region, and the other region was not. The ROS level of different regions was then investigated by confocal laser scanning microscopy (CLSM) imaging.

2.7. In Vitro Cytotoxicity Assay. A549 and HeLa cancer cells at the concentration of 5000 per well were seeded in a 96-well plate with 100 μL media. After cells were incubated in a humidified atmosphere of 5% CO_2 at 37 °C for 12 h, a series of Fe_3O_4-NS-C_3N_4@mSiO_2-PEG-RGD species at different concentrations were added. After incubation for another 48 h, the cell viability was measured. For dual targeting chemo-photodynamic synergistic treatment, before adding anything, A549 and HeLa cancer cells at concentration of 5000 per well were incubated for 24 h. The bare Fe_3O_4-NS-C_3N_4@mSiO_2-PEG-RGD, DOX-loaded Fe_3O_4-NS-C_3N_4@mSiO_2-PEG, or DOX-loaded Fe_3O_4-NS-C_3N_4@mSiO_2-PEG-RGD was added at a concentration equivalent to free DOX. After incubation for 6 h, each well was washed twice by the PBS buffer to remove the nanocarrier or drug not uptaken by cells. Every line of wells was irradiated by visible light for 10 min at the wavelength of 450 nm in the vis-irradiated group (Fe_3O_4-NS-C_3N_4@mSiO_2-PEG-RGD/vis, Fe_3O_4-NS-C_3N_4@mSiO_2-PEG-RGD/DOX/vis, Fe_3O_4-NS-C_3N_4@mSiO_2-PEG-RGD/DOX/vis/Mag), and the other incubation conditions were the same as those in the non-vis-irradiated group (free DOX, Fe_3O_4-NS-C_3N_4@mSiO_2-PEG-RGD/DOX and Fe_3O_4-NS-C_3N_4@mSiO_2-PEG/DOX). After incubation for another 8 h, the cell viability was measured.

2.8. Survival States of A549 Cancer Cells under Optical Microscope Imaging. For the visual identification of survival states of A549 cancer cells after different treatment, experimental groups were stained with 0.4% Trypan blue for 5 min after different incubation conditions (Fe_3O_4-NS-C_3N_4@mSiO_2-PEG-RGD/vis, Fe_3O_4-NS-C_3N_4@mSiO_2-PEG-RGD/DOX/vis, Fe_3O_4-NS-C_3N_4@mSiO_2-PEG-RGD/DOX/vis/Mag, Fe_3O_4-NS-C_3N_4@mSiO_2-PEG-RGD/DOX, and Fe_3O_4-NS-C_3N_4@mSiO_2-PEG/DOX), followed by two washes with the PBS buffer. Images of cells were then taken under an optical microscope.

2.9. Characterizations. Transmission 30 electron microscopy (TEM) was conducted on a JEOL 2000 EX electronic microscope with an accelerating voltage of 120 keV. Fourier transformed infrared (FTIR) spectroscopy characterization was performed on a Thermo Nicolet 380 spectrometer using KBr pellets (Nicolet, WI). The nitrogen adsorption measurement was conducted at −196 °C (liquid nitrogen temperature) using a static-volumetric method on ASAP 2010 (Micromeritics). Pore diameter and distribution curves were calculated by the BJH (Barrett−Joyner−Halenda) method from adsorption branch. UV−vis spectra were recorded on a UV-3101PC Shimadzu spectroscope. The confocal laser scanning microscopy (CLSM) imaging was performed by a FluoViewTM FV1000 confocal laser scanning microscope (Olympus) with an 100× objective. Cells were preplanted in the glass-bottom dishes (NEST). Optical images were taken under an Olympus CKX 41 microscope (Olympus). Powder X-ray diffraction patterns of the samples were collected on a Bruker D8FOCUS X-ray diffractometer. The saturation magnetization curve was obtained at room temperature on a Physical Property Measurement System 9T (Quantum Design, San Diego). EDS element analysis was conducted on the Inca X-Max80 EDS system (Oxford).

3. RESULTS AND DISCUSSION

The process for the fabrication of the multifunctional nancarrier was illustrated in Figure 1. First, C_3N_4 nanosheets (NS-C_3N_4) were synthesized through heat polymerization of melamine coupled with repeated ultrasonication and centrifugation based on a previous study.[10] Then, a solvothermal reaction was conducted to decorate Fe_3O_4 nanoparticles onto NS-C_3N_4 (Fe_3O_4-NS-C_3N_4). Under the direction of surfactant CTAB, the mesoporous silica shell was subsequently assembled onto Fe_3O_4-NS-C_3N_4 (Fe_3O_4-NS-C_3N_4@mSiO_2). Finally, a PEG linker was utilized to connect Fe_3O_4-NS-C_3N_4@mSiO_2 with the RGD targeting peptide (Fe_3O_4-NS-C_3N_4@mSiO_2-PEG-RGD). On the basis of TEM results, after repeated ultrasonication and centrifugation to remove unexfoliated bulk C_3N_4, the size of NS-C_3N_4 was decreased to 100−200 nm (Figure 2a and Supporting Information Figure S1), suitable for the intracellular application. Also, the nearly translucent feature of NS-C_3N_4 solution also demonstrated the material's ultrathin thickness, further identifying the successful exfoliation of bulk C_3N_4 (Supporting Information Figure S2). According to previous studies,[10,44,45] the effective exfoliation of bulk C_3N_4 would enhance the fluorescent and photocatalytic ability of C_3N_4 to enable NS-C_3N_4 as a potential imaging as well as photodynamic agent. Moreover, it was also reported the decoration of NS-C_3N_4 with metal or metal oxide nanoparticles could enhance its ability to generate ROS under visible light irradiation through the increase of separation efficiency of photogenerated electron−hole pairs, which we assumed would benefit the PDT effect.[31,32,36−38] Given this, among these nanoparticles here we chose Fe_3O_4 nanoparticles as the accessory to decorate NS-C_3N_4, not only for the enhanced generation of ROS under visible light irradiation, but also for an additional arrival of the magnetic response to endow the nanocarrier with a magnetic targeting ability. Numerous Fe_3O_4 nanoparticles were dotted

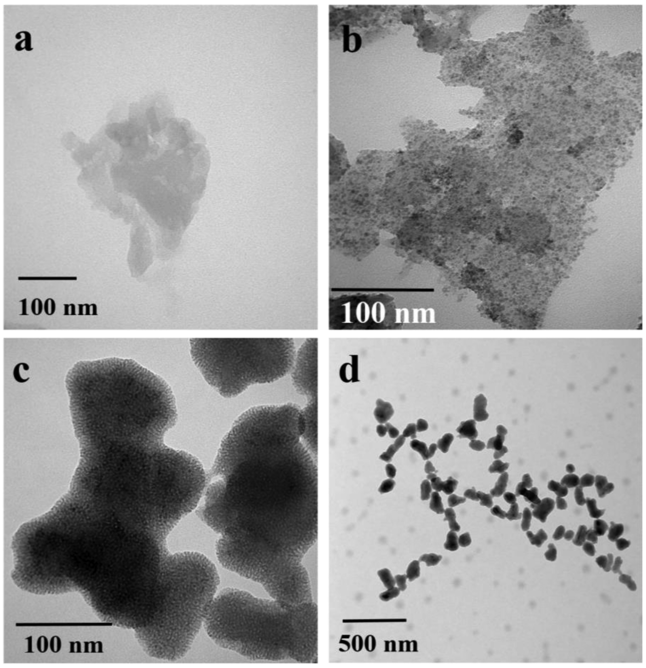

Figure 2. TEM images of (a) NS-C_3N_4, (b) Fe_3O_4-NS-C_3N_4, (c, d) Fe_3O_4-NS-C_3N_4@mSiO_2-PEG-RGD.

onto NS-C_3N_4 after the construction of a solvothermal reaction (Figure 2b). The zeta potential of as-synthesized NS-C_3N_4 was −31.5 mV at neutral condition (water solution) and became even more negative when the surrounding environment became more alkali. In view of the alkali condition for the assembly of the mesoporous silica shell, we assumed the electrostatic attraction between negative NS-C_3N_4 and positive structure director CTAB would facilitate the coating of a well-defined mesoporous silica shell onto Fe_3O_4-NS-C_3N_4. As expected, seen from Figure 2c,d, a clear mesoporous silica shell appeared once the sol−gel assembly was completed. As for XRD analysis, compared with bulk, C_3N_4, Fe_3O_4-NS-C_3N_4@mSiO_2 showed a much weaker peak resulting from the effective exfoliation at 27.4°, a broad peak between 20° and 30° corresponding to the amorphous silica shell, and diffraction peaks of Fe_3O_4, all of which further confirmed the successful fabrication of Fe_3O_4-NS-C_3N_4@mSiO_2 (Figure 3a). And EDS element analysis also illustrated the existing fundamental elements (Fe, Si, C, N, Figure 3b). In order to achieve the peptide-mediated targeting ability, a PEG linker, which could enhance the stability and dispersibility of the nanocarrier in the physiological condition, was then utilized to connect the RGD targeting peptide (specifically recognizing cancer cells overexpressing the integrin $\alpha_v\beta_3$) with Fe_3O_4-NS-C_3N_4@mSiO_2. Supported by FTIR analysis (Figure 3c), Fe_3O_4-NS-C_3N_4@mSiO_2 only showed characteristic peaks of the mesoporous silica shell (1084, 953, and 459 cm^{-1} correspond to ν_{as}Si−O−Si, ν_sSi−O−Si, and ρSi−O−Si, respectively), NS-C_3N_4 (fingerprint peaks within 1000−1900 cm^{-1}), and Fe_3O_4 (Fe−O, 580 cm^{-1}). While new peaks corresponding to C−H_x (2925, 2983 cm^{-1}) emerged for Fe_3O_4-NS-C_3N_4@mSiO_2-PEG-RGD the zeta potential measurement was auxiliary proof for the successful anchor of the RGD targeting peptide (Supporting Information Figure S3). To further directly confirm that the RGD targeting peptide was

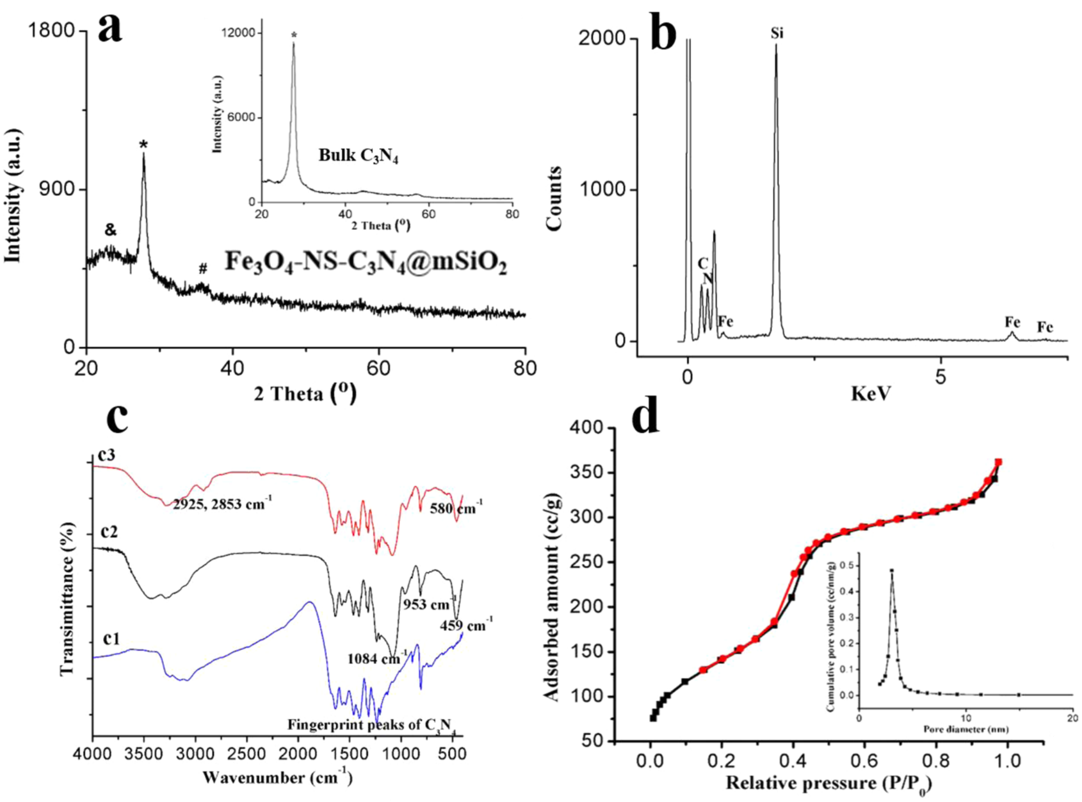

Figure 3. (a) XRD analysis of Fe_3O_4-NS-C_3N_4@mSiO_2 and bulk C_3N_4. *, &, and # indicate diffraction peaks of C_3N_4, amorphous silica, and magnetite phase of Fe_3O_4, respectively. (b) EDS element analysis of Fe_3O_4-NS-C_3N_4@mSiO_2. (c) FTIR analysis of (c1) NS-C_3N_4, (c2) Fe_3O_4-NS-C_3N_4@mSiO_2, and (c3) Fe_3O_4-NS-C_3N_4@mSiO_2-PEG-RGD. (d) BET and BJH analyses of Fe_3O_4-NS-C_3N_4@mSiO_2.

indeed anchored onto the mesoporous silica shell, we carried out a BCA assay. From Supporting Information Figure S4, it was clearly observed at a determined time only Fe_3O_4-NS-C_3N_4 or Fe_3O_4-NS-C_3N_4@$mSiO_2$-NH_2 would not change the color of BCA solution. However, the color turned into purple and even became darker when the amount of the anchored RGD targeting peptide increased. Finally, a N_2 adsorption experiment was used to probe the detailed structure information on Fe_3O_4-NS-C_3N_4@$mSiO_2$. The nitrogen adsorption−desorption isotherm of Fe_3O_4-NS-C_3N_4@$mSiO_2$ showed a typical IV isotherm pattern of the mesoporous material and a characteristic adsorption step in the 0.1−0.3 relative pressure range, which hinted that the nanocarrier possessed a narrow distribution of pore size (Figure 3d). According to results of BET and BJH analyses, the nanocarrier exhibited high surface area of 516.726 m^2/g and large pore volume of 0.569 cc/g with the main pore diameter distributed around 3.058 nm, implying a potentially high loading capacity for the anticancer drug. It is worth mentioning that the as-prepared nanoparticles are quite stable which could be stored in the aqueous environment for at least 5 days or a much longer time in the dry state.

Fe_3O_4-NS-C_3N_4@$mSiO_2$-PEG-RGD was supposed to be the pH-responsive nanocarrier, and its "on-demand" release pattern was then evaluated. The loading capacity of this nanocarrier toward DOX (a model drug for cancer treatment) could reach as high as 0.552 ± 0.20 g/g, which may result from synergistic loading of DOX by NS-C_3N_4 and pore channels of $mSiO_2$. Then, the release behavior of DOX from Fe_3O_4-NS-C_3N_4@$mSiO_2$-PEG-RGD was carefully investigated at various pH values (4.5, 5.5, and 7.4). Shown as Figure 4, at lower pH (4.5 or 5.5), mimicking the microenvironment of cancer cells, both the release speed and release amount of DOX were higher than those in the case of pH = 7.4 (mimicking the microenvironment of normal cells). To probe the underlying mechanism, a zeta potential experiment was conducted. In detail, when the pH was 7.4, the zeta potential of NS-C_3N_4 was −10.7 mV. If the pH decreased to 5.5 or 4.5, the zeta potential of NS-C_3N_4 would increase to −2.8 or 3.27 mV, respectively (all zeta potential measurements were conducted in the PBS buffer). Many researchers have already indicated the low pH would protonate the DOX which would enhance its solubility in the aqueous environment, leading to an enhanced release from the nanocarrier.[46,47] In the meantime, we speculated that, in consideration of the permanent positive zeta potential of DOX (pK_a = 8. 2) at the experimental conditions, strongly electronegative NS-C_3N_4 and $mSiO_2$ would attract electropositive DOX when the surrounding pH was 7.4, preventing a burst release. If the surrounding pH decreased to 5.5 or 4.5, the weak electrostatic attraction or the electrorepulsive force among $mSiO_2$, NS-C_3N_4, and DOX combined with the enhanced water solubility of DOX attributed to the protonation effect would accelerate the release of DOX, realizing the pH-triggered release pattern for the "on-demand" administration.

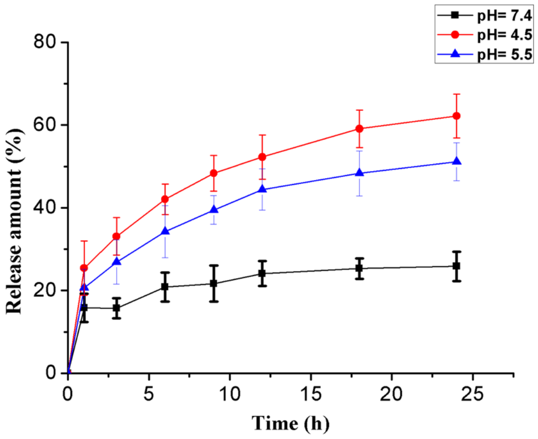

Figure 4. Release of loaded DOX in 24 h from Fe_3O_4-NS-C_3N_4@$mSiO_2$-PEG-RGD at various pH values: (black curve) 7.4, (blue curve) 5.5, and (red curve) 4.5.

Fe_3O_4-NS-C_3N_4@$mSiO_2$-PEG-RGD with the autoflurescence was meant to be facilely tracked within cells. However, the decoration of NS-C_3N_4 with Fe_3O_4 nanoparticles would quench the fluorescent ability of NS-C_3N_4 to some extent. Shown as Supporting Information Figure S5, the more Fe_3O_4 nanoparticles were dotted, the more fluorescence was quenched. In order to make Fe_3O_4-NS-C_3N_4@$mSiO_2$-PEG-RGD still suitable for intracellular imaging, the amount of Fe_3O_4 nanoparticles should be strictly controlled. After a series of optimizations, the obtained Fe_3O_4-NS-C_3N_4@$mSiO_2$-PEG-RGD was sufficiently bright to image cells but also with a moderate magnetic response (a saturation magnetization value of 4 emu/g, Supporting Information Figure S6) for a preconceived magnetic targeting ability. Attributed to ultrahigh photostability shown in Supporting Information Figure S7, the resultant Fe_3O_4-NS-C_3N_4@$mSiO_2$-PEG-RGD was superbly suitable for a long-term live-cell track, which remained stable and strongly fluorescent in at least 3 h UV irradiation in sharp contrast to conventional dyes, FITC, Lysotracker, and DOX whose fluorescent signals rapidly diminished in <2 h under the same condition.[48] To intuitionally identify the dual targeting (the peptide- and magnetism-mediated targeting) ability of Fe_3O_4-NS-C_3N_4@$mSiO_2$-PEG-RGD, two sets of A549 cells were incubated with Fe_3O_4-NS-C_3N_4@$mSiO_2$-PEG and Fe_3O_4-NS-C_3N_4@$mSiO_2$-PEG-RGD, respectively, for 3 or 6 h. In parallel, a third set of A549 cells was incubated with Fe_3O_4-NS-C_3N_4@$mSiO_2$-PEG-RGD under the magnetic attraction. On the basis of CLSM results (Figure 5, blue channel), the uptakes of Fe_3O_4-NS-C_3N_4@$mSiO_2$-PEG-RGD and Fe_3O_4-NS-C_3N_4@$mSiO_2$-PEG by A549 cancer cells were both positively related to the incubation time, of which more nanocarriers could be taken in at a longer incubation time. Meanwhile, at the same incubation time, the intracellular fluorescent density was stronger in the case of Fe_3O_4-NS-C_3N_4@$mSiO_2$-PEG-RGD than that in the case of Fe_3O_4-NS-C_3N_4@$mSiO_2$-PEG. In detail, the RGD targeting peptide could specifically recognize the integrin $\alpha_v\beta_3$ receptor overexpressed on the membrane surface of A549 cancer cells, promoting the internalization of the nanocarrier, which identified the peptide-mediated targeting ability. When a magnet was applied, Fe_3O_4-NS-C_3N_4@$mSiO_2$-PEG-RGD was attracted toward cells to enhance the interaction for the facilitation of internalization, reflected by the stronger intracellular fluorescence compared with the case without the magnetic attraction to confirm the magnetic targeting ability. It was recently reported that NS-C_3N_4 demonstrated a good two-photon adsorption (TPA) ability, which could simultaneously absorb two near-infrared photons and emit bright fluorescence in the visible light region. And the TPA cross section of NS-C_3N_4 has a maximum δ up to 28 000 GM at 750 nm, orders of magnitude larger than that of previously reported organic dyes.[34] Inspired by this, another CLSM experiment (Figure 5, green channel) similar to one-

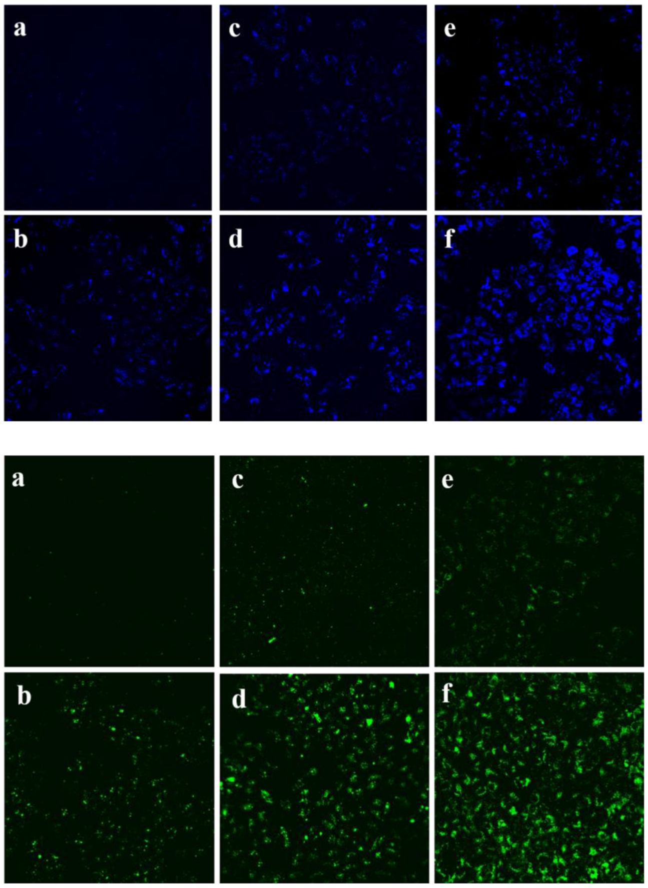

Figure 5. CLSM images of A549 cancer cells after incubation with (a, b) Fe_3O_4-NS-C_3N_4@mSiO_2-PEG, (c, d) Fe_3O_4-NS-C_3N_4@mSiO_2-PEG-RGD, and (e, f) Fe_3O_4-NS-C_3N_4@mSiO_2-PEG-RGD under the magnetic attraction for 3 (a, c, e) or 6 (b, d, f) h. Blue channel was conducted under 405 nm excitation, and green channel was conducted under 780 nm excitation.

photon imaging was conducted. Instead, this time was based on the two-photon excitation (780 nm). As expected, results were identical to one-photon imaging, demonstrating the robustness and feasibility of this nanocarrier for a two-photon imaging application, which was more suitable for in vivo imaging in the future.

To further quantatively demonstrate the dual targeting ability, flow cytometry was utilized to dissect the uptake of the nanocarrier by cells. Herein, A549 cancer cells (positively expressing $\alpha_v\beta_3$ receptor),[42] MCF-7 cancer cells (negatively expressing $\alpha_v\beta_3$ receptor),[49] and HK-2 normal cells (negatively expressing $\alpha_v\beta_3$ receptor)[50] were applied in parallel to incubate with different kinds of nanocarriers under various conditions. In the case of A549 cancer cells (Figure 6a), the uptake of Fe_3O_4-NS-C_3N_4@mSiO_2-PEG-RGD exceeded that of Fe_3O_4-NS-C_3N_4@mSiO_2-PEG by a great deal with respect to the comparable uptake of these two nanocarriers in both cases of MCF-7 cancer cells and HK-2 normal cells (Figure 6b,c), hinting at the existing peptide-mediated targeting. In the meantime, an increased uptake of Fe_3O_4-NS-C_3N_4@mSiO_2-PEG-RGD by all A549, MCF-7, and HK-2 cells was obviously observed when a magnet was applied during the incubation, identifying the magnetic targeting ability. On the whole, the flow cytometry experiment combined with the aforementioned CLSM assay provided strong evidence for the dual targeting ability of Fe_3O_4-NS-C_3N_4@mSiO_2-PEG-RGD.

Graphite carbon nitride (g-C_3N_4) with a bandgap of 2.7 eV has been reported as an excellent photocatalytic agent (using ROS generated under light irradiation to degrade substances) by many researchers. Also, the effective exfoliation and Fe_3O_4 nanoparticle decoration of g-C_3N_4 would enhance its ability to generate ROS under visible light irradiation,[10,31,32,44,45] which we assumed would make Fe_3O_4-NS-C_3N_4@mSiO_2-PEG-RGD as a potential photodynamic agent, enabling PDT. To identify this assumption, the intracellular ROS level of cells treated with Fe_3O_4-NS-C_3N_4@mSiO_2-PEG-RGD under visible light irradiation was evaluated by CLSM. After sufficient incubation with Fe_3O_4-NS-C_3N_4@mSiO_2-PEG-RGD and 2,7-dichlorouorescein (DCFH) (a ROS probe which did not emit fluorescence but emitted strong green fluorescence once oxidized by ROS), A549 cancer cells were irradiated by visible light at the wavelength of 450 nm ($40\ \text{mW/cm}^{-2}$) or not. Shown as Figure 7, cells in the group with irradiation emitted strong green fluorescence with respect to weak green fluorescence in the group without irradiation, reflecting the efficient ROS generation ability of Fe_3O_4-NS-C_3N_4@mSiO_2-PEG-RGD under visible light irradiation. Moreover, the confined beam of visible light could also provide site-targeted treatment, which might reduce severe damage toward normal cells during administration. Following this consumption, visible light was constrained to irradiate only one part of the well. Obviously, a boundary emerged in CLSM images (Figure 7e), of which cells in the part with visible light irradiation emitted strong green fluorescence while surrounding cells showed negligible fluorescence, demonstrating the different intracellular ROS

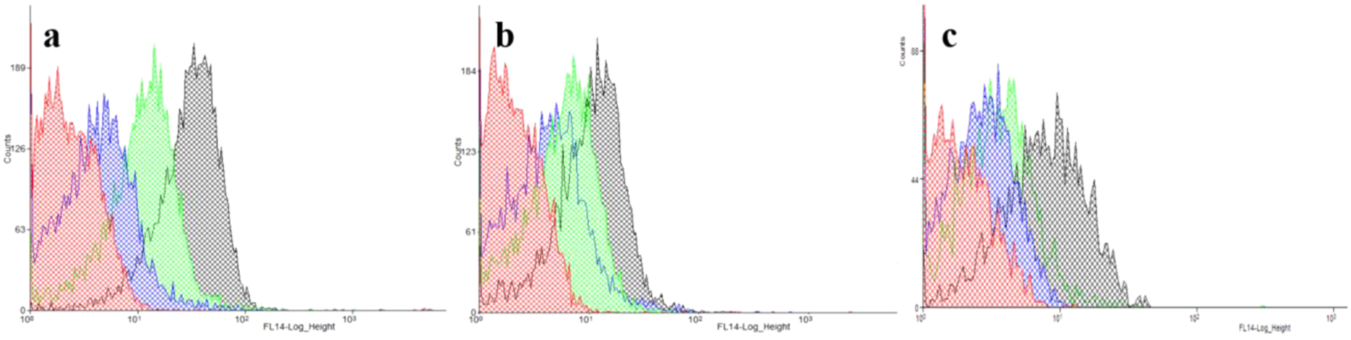

Figure 6. Flow cytometry analysis of (a) A549 cancer cells, (b) MCF-7 cancer cells, and (c) HK-2 normal cells incubated with different kinds of nanocarriers under various conditions. Red, blue, green, and black diagrams correspond to groups of control, Fe_3O_4-NS-C_3N_4@mSiO_2-PEG, Fe_3O_4-NS-C_3N_4@mSiO_2-PEG-RGD, and Fe_3O_4-NS-C_3N_4@mSiO_2-PEG-RGD under the magnetic attraction, respectively.

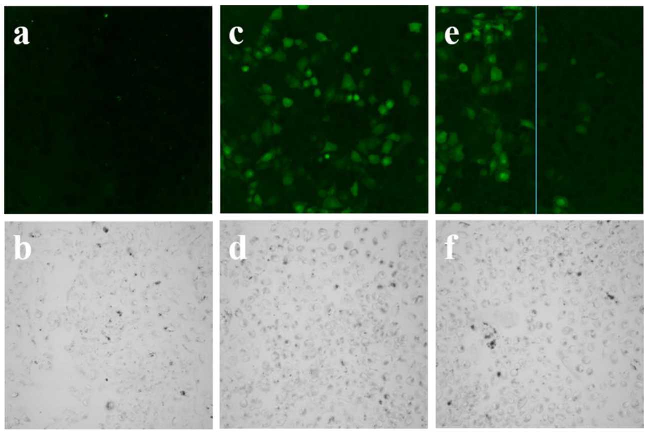

Figure 7. Intracellular ROS detection of A549 cancer cells incubated with Fe_3O_4-NS-C_3N_4@mSiO_2-PEG-RGD either (c) under visible light irradiation or (a) not; (e) site-targeted PDT. Parts b, d, and f correspond to the optical images of a, c, and e.

level between these two parts of cells to confirm site-targeted treatment.

Given all aforementioned demonstrations, Fe_3O_4-NS-C_3N_4@mSiO_2-PEG-RGD was supposed to be the excellent nanocarrier with dual targeting chemo-photodynamic synergistic treatment, and the in vitro assay was then systematically investigated. At first, the cytotoxicity of bare Fe_3O_4-NS-C_3N_4@mSiO_2-PEG-RGD toward A549 and HeLa cancer cells (all overexpressing $\alpha_v\beta_3$ receptor)[51] was evaluated. Shown in Figure 8, even if the concentration of Fe_3O_4-NS-C_3N_4@mSiO_2-PEG-RGD remained as high as 250 μg/mL, the cell viability was still up to 91.94% for A549 cancer cells and 90.78% for HeLa cancer cells after 48 h incubation, validating the negligible cytotoxicity of Fe_3O_4-NS-C_3N_4@mSiO_2-PEG-RGD. On account of the ability of generation of ROS under visible light irradiation, Fe_3O_4-NS-C_3N_4@mSiO_2-PEG-RGD would realize intracellular PDT. First, the negligible photoxicity of visible light at the experimental condition was proven (vis alone, Figure 9a,b, dark blue bar). Inspired by this, a PDT experiment was subsequently conducted (Fe_3O_4-NS-C_3N_4@mSiO_2-PEG-RGD/vis). After incubation with Fe_3O_4-NS-C_3N_4@mSiO_2-PEG-RGD at a determined time, cells were irradiated at the wavelength of 450 nm for 10 min. It was obviously found that all experimental groups showed some extent cell death, and the PDT efficacy exhibited a dose-dependent manner (Figure 9a,b, light blue bar). What was worth mentioning was the cell viability decreased to as low as 62.17% and 71.10% for A549 and HeLa cancer cells, respectively, when the applied concentration of Fe_3O_4-NS-C_3N_4@mSiO_2-PEG-RGD reached 60 μg/mL, demonstrating efficient PDT. Fe_3O_4-NS-C_3N_4@mSiO_2-PEG-RGD could load DOX and selectively delivered it to cancer cells for the administration of chemotherapy (Fe_3O_4-NS-C_3N_4@mSiO_2-PEG-RGD/DOX). After overnight loading of DOX, Fe_3O_4-NS-C_3N_4@mSiO_2-PEG-RGD and Fe_3O_4-NS-C_3N_4@mSiO_2-PEG (Fe_3O_4-NS-C_3N_4@mSiO_2-PEG/DOX) were applied in parallel to incubate with A549 and HeLa cancer cells. To figure out the subcellular localization of the nanocomposite after internalization, Lysotracker probe was used to stain the acidic organelles. Shown as Supporting Information Figure S8, the nanocarrier was mostly trapped within lysosome or endosome, reflected by the yellow merged spots which were a result of overlap between green (Fe_3O_4-NS-C_3N_4@mSiO_2-PEG-RGD) and red (Lysotracker) spots. We speculated the low pH environment in lysosome or endosome would trigger the release of DOX, and the released DOX subsequently diffused into the nucleus to inhibit the synthesis of nucleic acid which finally led to cell apoptosis. Consistent with the consumption, either Fe_3O_4-NS-C_3N_4@mSiO_2-PEG-RGD/DOX or Fe_3O_4-NS-C_3N_4@mSiO_2-PEG/DOX exhibited efficient chemotherapy and also showed a dose-dependent manner. Specifically, compared with Fe_3O_4-NS-C_3N_4@mSiO_2-PEG/DOX, Fe_3O_4-NS-C_3N_4@mSiO_2-PEG-RGD/DOX expressed the more efficient chemotherapy at every amount attributed to the enhancement of internalization of the nanocarrier by cells mediated by the RGD targeting peptide as described above (Figure 9a,b, black and red bars). In view of the above efficient chemotherapy and PDT, we assumed the combination of these two modalities of treatment might generate a synergistic effect to eventually improve the therapeutic efficacy (Fe_3O_4-NS-C_3N_4@mSiO_2-PEG-RGD/DOX/vis). After internalization of Fe_3O_4-NS-C_3N_4@mSiO_2-PEG-RGD with loaded DOX, chemotherapy would be activated just as described above, and at the same time cells were irradiated by visible light to activate PDT. Compared with sole chemotherapy or PDT, at every amount synergistic treatment demonstrated the better therapeutic efficacy, implying the high potency to combat cancer (Figure 9a,b, pink bar). And when a magnetic force was applied during the incubation, synergistic treatment exhibited even better therapeutic efficacy, which could be explained by the greater uptake of the nanocarrier by cells that contributed from the

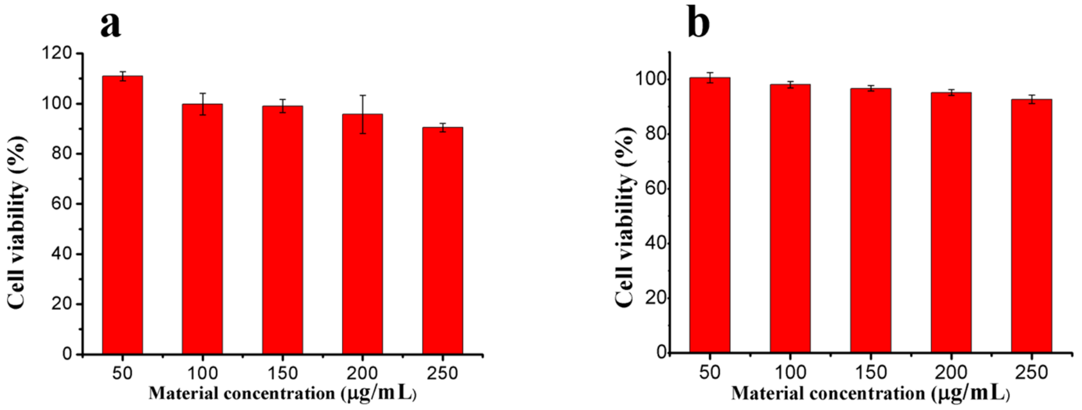

Figure 8. Cytotoxicity of bare Fe_3O_4-NS-C_3N_4@mSiO_2-PEG-RGD toward (a) A549 and (b) HeLa cancer cells after incubation for 48 h.

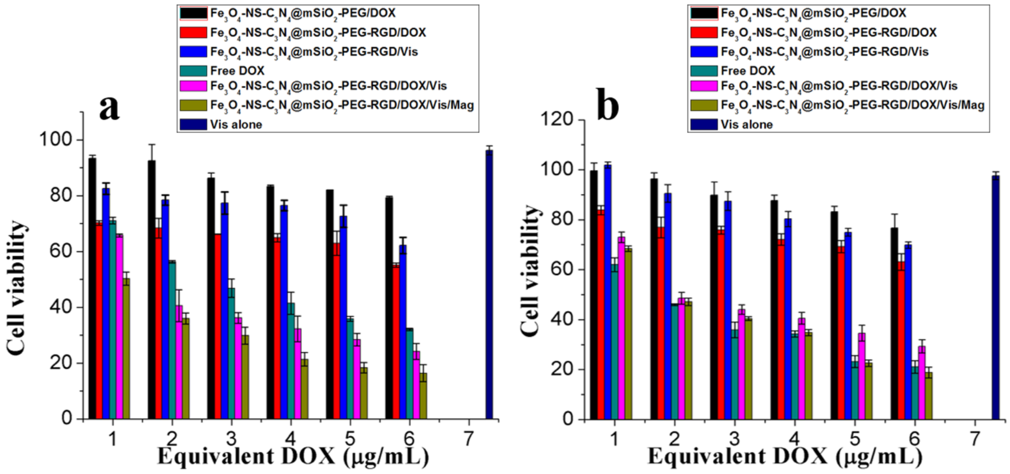

Figure 9. Cell viability of (a) A549 and (b) HeLa cancer cells under conditions of Fe_3O_4-NS-C_3N_4@mSiO_2-PEG/DOX (black bar), Fe_3O_4-NS-C_3N_4@mSiO_2-PEG-RGD/DOX (red bar), Fe_3O_4-NS-C_3N_4@mSiO_2-PEG-RGD/vis (light blue bar), free DOX (green bar), Fe_3O_4-NS-C_3N_4@mSiO_2-PEG-RGD/DOX/vis (pink bar), Fe_3O_4-NS-C_3N_4@mSiO_2-PEG-RGD/DOX/vis/Mag (brown bar), and vis alone (dark blue bar).

dual targeting ability as mentioned above (Figure 9a,b, brown bar). To further identify efficient dual targeting synergistic treatment (Fe_3O_4-NS-C_3N_4@mSiO_2-PEG-RGD/DOX/vis/Mag), free DOX at the equivalent amount of loaded DOX within Fe_3O_4-NS-C_3N_4@mSiO_2-PEG-RGD was incubated with A549 and HeLa cancer cells, respectively. Because of the direct administration toward cells, free DOX induced more cell death than either treatment alone (Figure 9a,b, green bar). However, as for dual targeting synergistic treatment, the therapeutic efficacy overmatched that of free DOX at every amount in the case of A549 cancer cells and approached toward that of free DOX with the eventual overmatch in the case of HeLa cancer cells. As another piece of evidence, the feasibility of Fe_3O_4-NS-C_3N_4@mSiO_2-PEG-RGD for dual targeting synergistic treatment was also evaluated via the observation of survival states of A549 cancer cells treated under different conditions by optical microscopy, in which dead cells were selectively stained with Trypan blue (Figure 10). Intuitionally, cells were partially killed under Fe_3O_4-NS-C_3N_4@mSiO_2-PEG/DOX, followed by the modest killing efficacy of Fe_3O_4-NS-C_3N_4@mSiO_2-PEG-RGD/DOX and Fe_3O_4-NS-C_3N_4@mSiO_2-PEG-RGD/vis, respectively. Remarkably, cells were almost killed under the treatment of Fe_3O_4-NS-C_3N_4@mSiO_2-PEG-RGD/DOX/vis, and better therapeutic efficacy was obtained when a magnet was applied during treatment (Fe_3O_4-NS-C_3N_4@mSiO_2-PEG-RGD/DOX/vis/Mag), all of which matched well with the aforementioned cell viability assay, reflecting efficient dual targeting synergistic treatment.

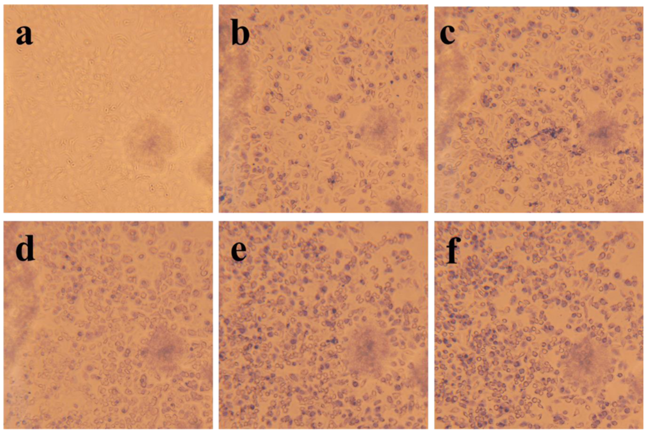

Figure 10. Survival states of A549 cancer cells under (a) vis alone, (b) Fe_3O_4-NS-C_3N_4@mSiO_2-PEG/DOX, (c) Fe_3O_4-NS-C_3N_4@mSiO_2-PEG-RGD/vis, (d) Fe_3O_4-NS-C_3N_4@mSiO_2@PEG-RGD/DOX, (e) Fe_3O_4-NS-C_3N_4@mSiO_2-PEG-RGD/DOX/vis, and (f) Fe_3O_4-NS-C_3N_4@mSiO_2-PEG-RGD/DOX/vis/Mag.

4. CONCLUSIONS

In summary, we elaborately fabricated the novel multifunctioal nanocarrier (Fe_3O_4-NS-C_3N_4@mSiO_2-PEG-RGD) by encapsulation of Fe_3O_4 nanoparticle-decorated NS-C_3N_4 within the mesoporous silica shell (mSiO_2) and the subsequent anchor of the RGD targeting peptide onto the outlet of mSiO_2, which was carefully characterized. As for the Fe_3O_4-NS-C_3N_4@mSiO_2-PEG-RGD multifunctional nanocarrier, the following details are relevant: First, NS-C_3N_4 with the autofluorescence enabled one- and two-photon imaging as well as combined with Fe_3O_4 nanoparticles to efficiently generate reactive oxygen species (ROS) under visible light irradiation for the demonstration of PDT. Second, mSiO_2 cooperated with NS-C_3N_4 to load anticancer drug for the realization of low pH-triggered chemotherapy and also enhanced the ability for further modification of the nanocarrier. Finally, the combination of Fe_3O_4 nanoparticles with the RGD targeting peptide endowed the nanocarrier with dual targeting ability to specifically centralize itself within cancer cells with the enhanced amount. Given all advances incorporated into the nanocarrier, Fe_3O_4-NS-C_3N_4@mSiO_2-PEG-RGD demonstrated the enhanced uptake by cancer cells and was facilely tracked within A549 cancer cells under one- and two-photon imaging. The efficient dual targeting chemo-photodynamic synergistic treatment of A549 and HeLa cancer cells by this novel multifunctional nanocarrier could lower the cell viability to 16.37% and 18.85%, respectively, which reflected the potency of Fe_3O_4-NS-C_3N_4@mSiO_2-PEG-RGD in cancer treatment.

■ ASSOCIATED CONTENT

Ⓢ Supporting Information

DLS analysis of NS-C_3N_4, photo of NS-C_3N_4 solution, zeta potential measurement, photos of BCA solution treated with Fe_3O_4-NS-C_3N_4@mSiO_2-PEG-RGD, photos of Fe_3O_4-NS-

C_3N_4@$mSiO_2$-PEG-RGD with different embedded Fe_3O_4 nanoparticles under irradiation of a UV hand lamp, room-temperature magnetization curve of Fe_3O_4-NS-C_3N_4@$mSiO_2$-PEG-RGD, photos of Fe_3O_4-NS-C_3N_4@$mSiO_2$-PEG-RGD solution under UV illustration for 1−3 h, and CLSM of subcellular localization of Fe_3O_4-NS-C_3N_4@$mSiO_2$-PEG-RGD. The Supporting Information is available free of charge on the ACS Publications website at DOI: 10.1021/acsami.5b01165.

AUTHOR INFORMATION

Corresponding Authors

*E-mail: weibingzhang@ecust.edu.cn.
*E-mail: hanfazou@dicp.ac.cn.

Author Contributions

The manuscript was written through contributions of all authors. All authors have given approval to the final version of the manuscript.

Notes

The authors declare no competing financial interest.

ACKNOWLEDGMENTS

This work was supported by the China State Key Basic Research Program Grant (2013CB911202, 2012CB910101, 2012CB910604), the Creative Research Group Project of NSFC (21321064), the National Natural Science Foundation of China (21235006, 81161120540), National Key Special Program on Infection Diseases (2012ZX10002009-011), and Analytical Method Innovation Program of MOST (2012IM030900).

REFERENCES

(1) Li, Z.; Yin, S.; Cheng, L.; Yang, K.; Li, Y.; Liu, Z. Magnetic Targeting Enhanced Theranostic Strategy Based on Multimodal Imaging for Selective Ablation of Cancer. *Adv. Funct. Mater.* **2014**, *24*, 2312−2321.

(2) Xu, C.; Yang, D. R.; Mei, L.; Li, Q. H.; Zhu, H. Z.; Wang, T. H. Targeting Chemophotothermal Therapy of Hepatoma by Gold Nanorods/Graphene Oxide Core/Shell Nanocomposites. *ACS Appl. Mater. Interfaces* **2013**, *5*, 12911−12920.

(3) Lin, L. S.; Cong, Z. X.; Cao, J. B.; Ke, K. M.; Peng, Q. L.; Gao, J. H.; Yang, H. H.; Liu, G.; Chen, X. Y. Multifunctional Fe_3O_4@ Polydopamine Core-Shell Nanocomposites for Intracellular mRNA Detection and Imaging-Guided Photothermal Therapy. *ACS Nano* **2014**, *8*, 3876−3883.

(4) Liu, X. J.; Marangon, I.; Melinte, G.; Wilhelm, C.; Moyon, C. M.; Pichon, P. B.; Ersen, O.; Aubertin, K.; Baaziz, W.; Huu, C. P.; Colin, S. B.; Bianco, A.; Gazeau, F.; Begin, D. Design of Covalently Functionalized Carbon Nanotubes Filled with Metal Oxide Nanoparticles for Imaging, Therapy, and Magnetic Manipulation. *ACS Nano* **2014**, *11*, 11290−11304.

(5) Zhang, Y.; Hu, Z.; Xu, G.; Gao, C.; Wu, R. a.; Zou, H. Elevating Mitochondrial Reactive Oxygen Species by Mitochondria-Targeted Inhibition of Superoxide Dismutase with A Mesoporous Silica Nanocarrier for Cancer Therapy. *Nano Res.* **2014**, *7*, 1103−1115.

(6) Li, W. P.; Liao, P. Y.; Su, C. H.; Yeh, C. S. Formation of Oligonucleotide-Gated Silica Shell-Coated Fe_3O_4-Au Core-Shell Nanotrisoctahedra for Magnetically Targeted and Near-Infrared Light-Responsive Theranostic Platform. *J. Am. Chem. Soc.* **2014**, *136*, 10062−10075.

(7) Choi, Y.; Kim, S.; Choi, M.-H.; Ryoo, S.-R.; Park, J.; Min, D.-H.; Kim, B.-S. Highly Biocompatible Carbon Nanodots for Simultaneous Bioimaging and Targeted Photodynamic Therapy In Vitro and In Vivo. *Adv. Funct. Mater.* **2014**, *24*, 5781−5789.

(8) Hong, G.; Robinson, J. T.; Zhang, Y.; Diao, S.; Antaris, A. L.; Wang, Q.; Dai, H. In Vivo Fluorescence Imaging with Ag_2S Quantum Qots in the Second Near-Infrared Region. *Angew. Chem., Int. Ed.* **2012**, *51*, 9818−9821.

(9) Wang, W.; Li, Y.; Cheng, L.; Cao, Z.; Liu, W. Water-Soluble and Phosphorus-Containing Carbon Dots with Strong Green Fluorescence for Cell Labeling. *J. Mater. Chem. B* **2014**, *2*, 46−48.

(10) Zhang, X.; Xie, X.; Wang, H.; Zhang, J.; Pan, B.; Xie, Y. Enhanced Photoresponsive Ultrathin Graphitic-Phase C_3N_4 Nanosheets for Bioimaging. *J. Am. Chem. Soc.* **2013**, *135*, 18−21.

(11) Dong, B.; Li, C.; Chen, G.; Zhang, Y.; Zhang, Y.; Deng, M.; Wang, Q. Facile Synthesis of Highly Photoluminescent Ag_2Se Quantum Dots as A New Fluorescent Probe in the Second Near-Infrared Window for in Vivo Imaging. *Chem. Mater.* **2013**, *25*, 2503−2509.

(12) Guo, L.; Wong, M. S. Multiphoton Excited Fluorescent Materials for Frequency Upconversion Emission and Fluorescent Probes. *Adv. Mater.* **2014**, *26*, 5400−5428.

(13) Qian, J.; Wang, D.; Cai, F.; Zhan, Q.; Wang, Y.; He, S. Photosensitizer Encapsulated Organically Modified Silica Nanoparticles for Direct Two-Photon Photodynamic Therapy and in Vivo Functional Imaging. *Biomaterials* **2012**, *33*, 4851−4860.

(14) Yan, H.; He, L.; Zhao, W.; Li, J.; Xiao, Y.; Yang, R.; Tan, W. Poly beta-Cyclodextrin/TPdye Nanomicelle-Based Two-Photon Nanoprobe for Caspase-3 Activation Imaging in Live Cells and Tissues. *Anal. Chem.* **2014**, *86*, 11440−11450.

(15) Curoissant, J.; Maynadier, M.; Mongin, O.; Hugues, V.; Blanchard-Desce, M.; Chaix, A.; Cattoen, X.; Wong Chi Man, M.; Gallud, A.; Gary-Bobo, M.; Garcia, M.; Raehm, L.; Durand, J. O. Enhanced Two-Photon Fluorescence Imaging and Therapy of Cancer Cells via Gold@Bridged Silsesquioxane Nanoparticles. *Small* **2015**, *11*, 295−299 DOI: 10.1002/smll.201401759.

(16) Kim, S.; Ohulchanskyy, Y. T.; Pudavar, E. H.; Pandey, K. R.; Prasad, N. P. Organically Modified Silica Nanoparticles Co-encapsulating Photosensitizing Drug and Aggregation-Enhanced Two-Photon Adsorbing Fluorescent Dye Aggreagates for Two-Photon Photodynamic Therapy. *J. Am. Chem. Soc.* **2007**, *129*, 2669−2675.

(17) Wan, H.; Zhang, Y.; Liu, Z.; Xu, G.; Huang, G.; Ji, Y.; Xiong, Z.; Zhang, Q.; Dong, J.; Zhang, W.; Zou, H. Facile Fabrication of A Near-Infrared Responsive Nanocarrier for Spatiotemporally Controlled Chemo-Photothermal Synergistic Cancer Therapy. *Nanoscale* **2014**, *6*, 8743−8753.

(18) Yavuz, M. S.; Cheng, Y.; Chen, J.; Cobley, C. M.; Zhang, Q.; Rycenga, M.; Xie, J.; Kim, C.; Song, K. H.; Schwartz, A. G.; Wang, L. V.; Xia, Y. Gold Nanocages Covered by Smart Polymers for Controlled Release with Near-Infrared Light. *Nat. Mater.* **2009**, *8*, 935−939.

(19) Yoon, S.; Kim, W. J.; Yoo, H. S. Dual-Responsive Breakdown of Nanostructures with High Doxorubicin Payload for Apoptotic Anticancer Therapy. *Small* **2013**, *9*, 284−293.

(20) Zhu, Y.; Shi, J.; Shen, W.; Dong, X.; Feng, J.; Ruan, M.; Li, Y. Stimuli-Responsive Controlled Drug Release from A Hollow Mesoporous Silica Sphere/Polyelectrolyte Multilayer Core-Shell Structure. *Angew. Chem., Int. Ed.* **2005**, *44*, 5083−5087.

(21) Sun, Y. L.; Yang, Y. W.; Chen, D. X.; Wang, G.; Zhou, Y.; Wang, C. Y.; Stoddart, J. F. Mechanized Silica Nanoparticles Based on Pillar[5]arenes for On-Command Cargo Release. *Small* **2013**, *9*, 3224−3229.

(22) Li, S.; Zheng, J.; Chen, D.; Wu, Y.; Zhang, W.; Zheng, F.; Cao, J.; Ma, H.; Liu, Y. Yolk-Shell Hybrid Nanoparticles with Magnetic and pH-Sensitive Properties for Controlled Anticancer Drug Delivery. *Nanoscale* **2013**, *5*, 11718−11724.

(23) Peng, F.; Su, Y.; Ji, X.; Zhong, Y.; Wei, X.; He, Y. Doxorubicin-Loaded Silicon Nanowires for the Treatment of Drug-Resistant Cancer Cells. *Biomaterials* **2014**, *35*, 5188−5195.

(24) Zhang, G.; Chang, H.; Amatore, C.; Chen, Y.; Jiang, H.; Wang, X. Apoptosis Induction and Inhibition of Drug Resistant Tumor Growth in Vivo Involving Daunorubicin-Loaded Graphene−Gold Composites. *J. Mater. Chem. B* **2013**, *1*, 493−499.

(25) Pan, L.; Liu, J.; Shi, J. Intranuclear Photosensitizer Delivery and Photosensitization for Enhanced Photodynamic Therapy with Ultralow Irradiance. *Adv. Funct. Mater.* **2014**, *24*, 7318−7327.

(26) Liang, R.; Tian, R.; Ma, L.; Zhang, L.; Hu, Y.; Wang, J.; Wei, M.; Yan, D.; Evans, D. G.; Duan, X. A Supermolecular Photosensitizer with Excellent Anticancer Performance in Photodynamic Therapy. *Adv. Funct. Mater.* **2014**, *24*, 3144−3151.

(27) Dai, Y.; Xiao, H.; Liu, J.; Yuan, Q.; Ma, P.; Yang, D.; Li, C.; Cheng, Z.; Hou, Z.; Yang, P.; Lin, J. In Vivo Multimodality Imaging and Cancer Therapy by Near-Infrared Light-Triggered trans-Platinum Pro-Drug-Conjugated Upconverison Nanoparticles. *J. Am. Chem. Soc.* **2013**, *135*, 18920−18929.

(28) Fan, W.; Shen, B.; Bu, W.; Chen, F.; He, Q.; Zhao, K.; Zhang, S.; Zhou, L.; Peng, W.; Xiao, Q.; Ni, D.; Liu, J.; Shi, J. A Smart Upconversion-based Mesoporous Silica Nanotheranostic System for Synergetic Chemo-/Radio-/Photodynamic Therapy and Simultaneous MR/UCL Imaging. *Biomaterials* **2014**, *35*, 8992−9002.

(29) Ren, H.; Wu, Y.; Li, Y.; Cao, W.; Sun, Z.; Xu, H.; Zhang, X. Visible-Light-Induced Disruption of Diselenide-Containing Layer-by-Layer Films: Toward Combination of Chemotherapy and Photodynamic Therapy. *Small* **2013**, *9*, 3981−3986.

(30) Yuan, Y.; Liu, J.; Liu, B. Conjugated-Polyelectrolyte-based Polyprodrug: Targeted and Image-Guided Photodynamic and Chemotherapy with on-Demand Drug Release upon Irradiation with A Single Light Source. *Angew. Chem., Int. Ed.* **2014**, *53*, 7163−7168.

(31) Zhou, X.; Jin, B.; Chen, R.; Peng, F.; Fang, Y. Synthesis of Porous Fe_3O_4/g-C_3N_4 Nanospheres as Highly Efficient and Recyclable Photocatalysts. *Mater. Res. Bull.* **2013**, *48*, 1447−1452.

(32) Kumar, S.; T, S.; Kumar, B.; Baruah, A.; Shanker, V. Synthesis of Magnetically Separable and Recyclable g-C_3N_4−Fe_3O_4 Hybrid Nanocomposites with Enhanced Photocatalytic Performance under Visible-Light Irradiation. *J. Phys. Chem. C* **2013**, *117*, 26135−26143.

(33) Zhang, X. L.; Zheng, C.; Guo, S. S.; Li, J.; Yang, H. H.; Chen, G. Turn-on Fluorescence Sensor for Intracellular Imaging of Glutathione Using g-C_3N_4 Nanosheet-MnO_2 Sandwich Nanocomposite. *Anal. Chem.* **2014**, *86*, 3426−3434.

(34) Zhang, X.; Wang, H.; Wang, H.; Zhang, Q.; Xie, J.; Tian, Y.; Wang, J.; Xie, Y. Single-Layered Graphitic-C_3N_4 Quantum Dots for Two-Photon Fluorescence Imaging of Cellular Nucleus. *Adv. Mater.* **2014**, *26*, 4438−4443.

(35) Lin, L.-S.; Cong, Z.-X.; Li, J.; Ke, K.-M.; Guo, S.-S.; Yang, H.-H.; Chen, G.-N. Graphitic-Phase C_3N_4 Nanosheets as Efficient Photosensitizers and pH-Responsive Drug Nanocarriers for Cancer Imaging and Therapy. *J. Mater. Chem. B* **2014**, *2*, 1031−1037.

(36) Li, Y.; Fang, L.; Jin, R.; Yang, Y.; Fang, X.; Xing, Y.; Song, S. Preparation and Enhanced Visible Light Photocatalytic Activity of Novel g-C_3N_4 Nanosheets Loaded with Ag_2CO_3 Nanoparticles. *Nanoscale* **2014**, *7*, 758−764.

(37) Cheng, N.; Tian, J.; Liu, Q.; Ge, C.; Qusti, A. H.; Asiri, A. M.; Al-Youbi, A. O.; Sun, X. Au-Nanoparticle-Loaded Graphitic Carbon Nitride Nanosheets: Green Photocatalytic Synthesis and Application Toward the Degradation of Organic Pollutants. *ACS Appl. Mater. Interfaces* **2013**, *5*, 6815−6819.

(38) Hong, J.; Yin, S.; Pan, Y.; Han, J.; Zhou, T.; Xu, R. Porous Carbon Nitride Nanosheets for Enhanced Photocatalytic Activities. *Nanoscale* **2014**, *6*, 14984−14990.

(39) Wang, Y.; Wang, K.; Zhao, J.; Liu, X.; Bu, J.; Yan, X.; Huang, R. Multifunctional Mesoporous Silica-Coated Graphene Nanosheet Used for Chemo-Photothermal Synergistic Targeted Therapy of Glioma. *J. Am. Chem. Soc.* **2013**, *135*, 4799−4804.

(40) Song, G.; Wang, Q.; Wang, Y.; Lv, G.; Li, C.; Zou, R.; Chen, Z.; Qin, Z.; Huo, K.; Hu, R.; Hu, J. A Low-Toxic Multifunctional Nanoplatform Based on Cu_9S_5@mSiO_2 Core-Shell Nanocomposites: Combining Photothermal- and Chemotherapies with Infrared Thermal Imaging for Cancer Treatment. *Adv. Funct. Mater.* **2013**, *23*, 4281−4292.

(41) He, L.; Huang, Y.; Zhu, H.; Pang, G.; Zheng, W.; Wong, Y.-S.; Chen, T. Cancer-Targeted Monodisperse Mesoporous Silica Nanoparticles as Carrier of Ruthenium Polypyridyl Complexes to Enhance Theranostic Effects. *Adv. Funct. Mater.* **2014**, *24*, 2754−2763.

(42) Shen, S.; Tang, H.; Zhang, X.; Ren, J.; Pang, Z.; Wang, D.; Gao, H.; Qian, Y.; Jiang, X.; Yang, W. Targeting Mesoporous Silica-Encapsulated Gold Nanorods for Chemo-Photothermal Therapy with Near-Infrared Radiation. *Biomaterials* **2013**, *34*, 3150−3158.

(43) Miura, Y.; Takenaka, T.; Toh, K.; Wu, S. R.; Nishihara, H.; Kano, R. M.; Ino, Y.; Nomoto, T.; Matsumoto, Y.; Koyama, H.; Cabral, H.; Nishiyama, N.; Kataoka, K. Cyclic RGD-Linked Polymeric Micelles for Targeted Delivery of Platinum Anticancer Drugs to Glioblastoma through the Blood-Brain Tumor Barrier. *ACS Nano* **2013**, *7*, 8583−8592.

(44) Yang, S.; Gong, Y.; Zhang, J.; Zhan, L.; Ma, L.; Fang, Z.; Vajtai, R.; Wang, X.; Ajayan, P. M. Exfoliated Graphitic Carbon Nitride Nanosheets as Efficient Catalysts for Hydrogen Evolution under Visible Light. *Adv. Mater.* **2013**, *25*, 2452−2426.

(45) Niu, P.; Zhang, L.; Liu, G.; Cheng, H.-M. Graphene-Like Carbon Nitride Nanosheets for Improved Photocatalytic Activities. *Adv. Funct. Mater.* **2012**, *22*, 4763−4770.

(46) Peng, F.; Su, Y. Y.; Wei, X. P.; Lu, Y. M.; Zhou, Y. F.; Zhong, Y. L.; Lee, S. T.; He, Y. Silicon-Nanowire-Based Nanocarriers with Ultrahigh Drug-Loading Capacity for In Vitro and In Vivo Cancer Therapy. *Angew. Chem., Int. Ed.* **2013**, *52*, 1457−1461.

(47) Liu, Z.; Sun, X. M.; Ratchford, N.; Dai, H. J. Supramolecular Chemistry on Water-Soluble Carbon Nanotubes for Drug Loading and Delivery. *ACS Nano* **2007**, *1*, 50−56.

(48) Ji, X.; Peng, F.; Zhong, Y.; Su, Y.; Jiang, X.; Song, C.; Yang, L.; Chu, B.; Lee, S. T.; He, Y., Highly Fluorescent, Photostable, and Ultrasmall Silicon Drug Nanocarriers for Long-Term Tumor Cell Tracking and In-Vivo Cancer Therapy. *Adv. Mater.* DOI: 10.1002/adma.201403848.

(49) Wang, S.; Chen, K. J.; Wu, T. H.; Wang, H.; Lin, W. Y.; Ohashi, M.; Chiou, P. Y.; Tseng, H. R. Photothermal Effects of Supramolecularly Assembled Gold Nanoparticles for the Targeted Treatment of Cancer Cells. *Angew. Chem., Int. Ed.* **2010**, *49*, 3777−3781.

(50) He, L. Z.; H, Y. Y.; Zhu, H. L.; Pang, G. H.; Zheng, W. J.; Wong, Y. S.; Chen, T. F. Cancer-Targeted Monodisperse Mesoporous Silica Nanoparticles as Carrier of Ruthenium Polypyridyl Complexes to Enhance Theranostic Effects. *Adv. Funct. Mater.* **2014**, *24*, 2754−2763.

(51) Pan, L. M.; Liu, J. N.; Shi, J. L. Intranuclear Photosensitizer Delivery and Photosensitization for Enhanced Photodynamic Therapy with Ultralow Irradiance. *Adv. Funct. Mater.* **2014**, *24*, 7318−7327.